

Denison University

Denison Digital Commons

Faculty Publications

2021

Tubular J-Aggregates of Cyanine Dyes in the Near-Infrared

Austin Bailey


Arundhati Deshmukh

Timothy Luke Atallah
Denison University

Ulugbek Barotov

Monica Pengshung

Follow this and additional works at: <https://digitalcommons.denison.edu/facultypubs>

 Part of the [Chemistry Commons](#)

Recommended Citation

Bailey, A., et al. (2021). Tubular J-aggregates of cyanine dyes in the near-infrared. <http://dx.doi.org/10.26434/chemrxiv-2021-rjmvz-v2>

This Article is brought to you for free and open access by Denison Digital Commons. It has been accepted for inclusion in Faculty Publications by an authorized administrator of Denison Digital Commons.

Exploring the Design of Superradiant J-Aggregates from Amphiphilic Monomer Units

Austin D. Bailey^[a], Arundhati P. Deshmukh^[a], Nadine C. Bradbury^[a], Monica Pengshung^[a], Timothy L. Atallah^[b], Jillian A. Williams^[a], Ulugbek Barotov^[c], Daniel Neuhauser^[a], Ellen M. Sletten^{*[a]}, and Justin R. Caram^{*[a]}

[a] Mr. Austin Bailey, Dr. Arundhati Deshmukh, Dr. Monica Pengshung, Jillian Williams, Nadine Bradbury, Dr. Ellen Sletten, Dr. Justin Caram
Department of Chemistry and Biochemistry
University of California Los Angeles
Los Angeles, CA, 90024
E-mail: jcaram@chem.ucla.edu, sletten@chem.ucla.edu

[b] Dr. Timothy Atallah
Department of Chemistry and Biochemistry
Denison University
Granville OH, 43023

[c] Mr. Ulugbek Barotov
Department of Chemistry
Massachusetts Institute of Technology
Cambridge, MA 02139

Abstract: Excitonic chromophore aggregates have wide-ranging applicability in fields such as imaging and energy harvesting, however their rational design requires adapting principles of self-assembly to the requirements of excited state coupling. Using the well-studied amphiphilic cyanine dye C8S3 as a template—known to assemble into tubular excitonic aggregates—we synthesize several redshifted variants and study their self-assembly and photophysics. The new pentamethine dyes retain their tubular self-assembly and demonstrate nearly identical bathochromic shifts and lineshapes well into near-infrared wavelengths. However, detailed photophysical analysis finds that the new aggregates show a significant decline in superradiance. Additionally, cryo-TEM reveals that these aggregates readily form short bundles of nanotubes that have nearly half the radii of their trimethine comparators. We employ computational screening to gain intuition on how the structural components of these new aggregates affect their excitonic states, finding that the narrower tubes are able to assemble into a larger number of arrangements, resulting in more disordered aggregates (i.e. less superradiant) with highly similar degrees of redshift.

Introduction

Excitonic molecular aggregates are non-covalently bound assemblies of organic chromophores known for their altered absorption and emission properties. The relative packing and arrangement of the dyes alters the excitonic/photophysical properties. For example a completely cofacial arrangement of dyes leads to an H-aggregate, a less emissive species blueshifted relative to the monomer, whereas a slipped arrangement of chromophores yields J-aggregates, a highly emissive species redshifted relative to the monomer.^{1,2} J-aggregates often display high cross-sections, increased radiative rates, and considerably redshifted emission making them well-suited for photophysical applications such as bioimaging or energy harvesting.³⁻⁶ Further, many polymethine-based J-aggregates manifest in 2D and quasi-2D supramolecular morphologies such as sheets, ribbons, or tubes.^{7,8} These extended structures often display highly narrowed and redshifted spectral features arising due to long-range excitonic coupling, facilitated by the increased chromophore density. These characteristics are also present in nature's most efficient photosynthetic systems,⁹⁻¹³ where tubular and ring aggregates couple extended excitonic states with directional energy flow.^{14,15}

We aimed to develop novel cyanine dyes that assemble into tubular J-aggregates (Figure 1a) with emission in the near-infrared (NIR, 700-1000 nm)¹⁶⁻¹⁸, a region where enhanced light penetration enables technological applications.¹⁹⁻²¹ To address this challenge, we modified the structure of an extant chromophore, known as 3,3'-bis(2-sulfopropyl)-5,5',6,6'-tetrachloro-1,1'-dioctylbenzimidacarbocyanine (Figure 1b, structure 1a), that forms superradiant tubular aggregates in the visible region. C8S3 was first introduced to the literature in 1997²² and has since been studied extensively as a model system for exciton transport, antenna effects, superradiance and quantum coherence.^{14,23-30} Recent work used synthetic modifications on the C8S3 monomer

to affect aggregation properties; larger halogen substitutions have been shown to increase the tube diameter, while placement of the halogen atoms was found to be critical in achieving H- vs. J-aggregation.^{31,32} We expand on this body of work by synthesizing elongated C8S3 dyes with redshifted absorption and emission.

The traditional method to bathochromically shift cyanine dyes is to increase the polymethine chain by one vinylene unit, thereby inducing nearly 3,000 cm⁻¹ (~100 nm) of redshift.³³ We use this method to design redshifted pentamethine dyes **2a** and **2b** (as opposed to trimethines **1a** and **1b** in the past) based on the C8S3 heterocycle, i.e. 3-(5,6-dichloro-2-methyl-1-octyl-1H-benzo[d]imidazol-3-ium-3-yl)propane-1-sulfonate. The pentamethine dyes aggregate similarly to their trimethine analogs, allowing us to access tubular aggregates of cyanine dyes with NIR emission. Additionally, we explore how that modification (i.e. trimethine to pentamethine) affects the self-assembly and photophysical properties of the aggregates through a combination of spectroscopy and computational screening.

Results and Discussion

The 3,3'-bis(2-sulfopropyl)-5,5',6,6'-tetrachloro-1,1'-dioctylbenzimidacarbocyanine (C8S3) heterocycles (**S5**, **S10**) and **1a/1b** were synthesized via a literature precedent.³¹ The pentamethine cyanines **2a** and **2b** were synthesized by heating the aforementioned heterocycle (**S5**, **S10**) and electrophilic linker (malonaldehyde bisphenylimine HCl) in the presence of a sterically hindered base (1,8-diazabicycloundecene, DBU) in dimethylformamide (Scheme S1). A heptamethine analog of the chlorine derivative was briefly investigated, but ultimately not pursued due to rapid degradation in methanol, which prevented aggregation and further characterization (Scheme S10, Figure S1).

In methanol, the pentamethine dye monomers absorb at $\lambda_{\text{max}} = 616 \text{ nm}$ (**2a**) and 614 nm (**2b**) as opposed to the trimethine dyes with $\lambda_{\text{max}} = 522 \text{ nm}$ (**1a**) and 523 nm (**1b**). Prior work on molecules **1a** and **1b** has shown that the two primary aggregate absorption features occur from the assembly of long double-walled nanotubes (DWNT) and the subsequent bundling of those nanotubes resulting in fibers of overlapping single-walled nanotubes. The DWNT produces several absorption peaks, with primary features at 599 nm and 589 nm , corresponding to the parallel transition of the inner and outer walls of the tube respectively.²⁶ Additionally, both the inner and outer wall show auxiliary features which have been assigned to the other parallel and perpendicular excitonic transitions, which are indicative of macroscopic exciton delocalization around each tubular structure.³⁴ The bundled nanotubes display a prominent parallel 603 nm feature but also have a second, broader absorption band around 580 nm .

To probe the aggregate morphologies of the new pentamethine dyes, we both screened **2a** and **2b** at varied concentrations while maintaining a constant methanol/water ratio (Figure 1c).³⁵ Aggregates of each chromophore were prepared by first creating a stock solution of the dye in methanol. To a small volume of this stock solution was added ultrapure H_2O . The final concentration and methanol/water ratio in each solution were varied. A complete procedure for preparing aggregates is included in SI Section 4. UV-Vis absorption was used to characterize the aggregates, which display a different spectral signature for each morphology.

In this exploration, we found that the pentamethine dye aggregates display similar photophysical properties to the trimethine dyes, forming two primary aggregates. We refer to these as a kinetic intermediate (KI) and bundles, though the analogous behaviour of **1a** suggests that the KI are transiently formed double-walled nanotubes (*vide infra*). We employed non-negative matrix factorization (NNMF), an algorithm which estimates the basis spectra corresponding to each

species in the binary solution, (Figure 1d) of the concentration series data in Figure 1c. At higher concentrations (>0.05 mM), the KI aggregates of **2a** rapidly converted to the “bundles”, a more redshifted species shown in Figure 1e. Figure 1f plots the mole fraction of each isolated aggregate as a function of concentration, showing that the two distinct aggregate morphologies can be prepared at 0.01 and 1 mM.

The KI aggregate of **2a** shows distinct features at 740 and 731 nm (achieved at low concentration, 0.01 mM, 10% methanol), while the bundles display broad absorption around 715 nm and retains the 745 nm feature (achieved at higher than 0.1 mM, 10% methanol). By analogy, we assign these to parallel and perpendicular polarized transitions.³⁴

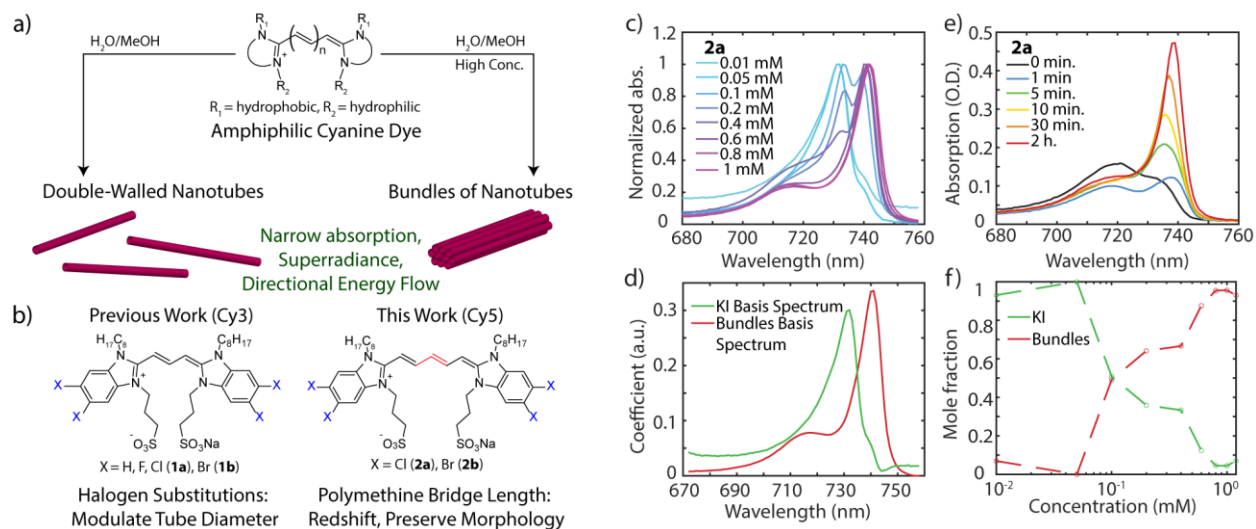


Figure 1 **a)** Self-assembly of amphiphilic cyanine dyes into J-aggregate nanostructures. **b)** Synthetic modifications on C8S3 (**1a**) in prior work (modifying halogen substitution/placement) and this work (trimethine to pentamethine). **c)** Normalized absorption of variable concentration samples of **2a**. All samples created using 10% MeOH, 90% H₂O using the procedure in SI section 4. **d)** Basis spectra for kinetic intermediate and bundles of **2a** achieved through non-negative matrix factorization of the concentration series in Figure 1c. **e)** Kinetic time series of a **2a** aggregate created at 10% MeOH, 90% H₂O and 0.05 mM dye. **f)** Plot of the normalized relative mole fraction of kinetic intermediate vs. bundles changing as a function of concentration.

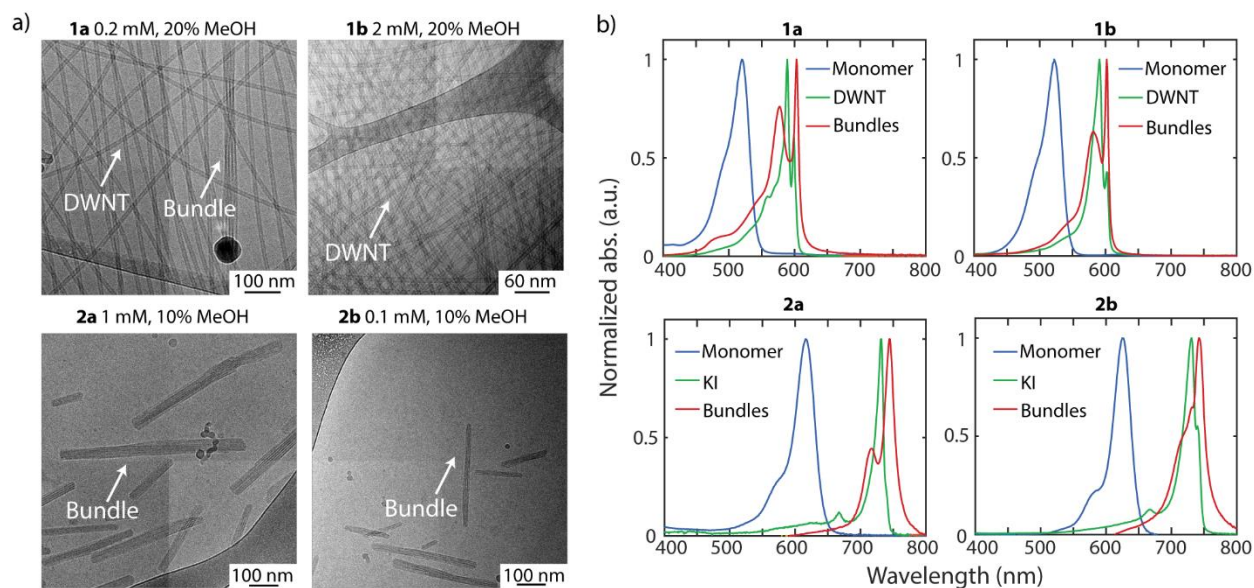


Figure 2. a) Cryo-electron microscopy images of trimethine double-walled nanotubes and pentamethine bundles b) Morphological characterization of monomers and aggregates of **1a**, **1b**, **2a**, and **2b**. Absorption spectrum of trimethine (**1a** and **1b**) and pentamethine (**2a** and **2b**) dye monomers (100% MeOH) and aggregates (DWNT = double-walled nanotube, KI = kinetic intermediate).

Upon identifying appropriate conditions for each aggregate with unique spectral signatures, we performed cryo-EM to determine their supramolecular morphologies. Cryo-EM for the bundled aggregate morphologies of **2a/2b** and DWNT morphologies of **1a/1b** is shown in Figure 2a; details on cryo-EM technique are in SI Section 6. Figure 2a confirms our assignments of the bundle aggregates of **2a** and **2b**. While the cryo-EM imaging of **2a** at high concentrations (>0.1 mM) clearly showed bundles analogous to **1a**, the aggregates prepared at 0.01 mM (stabilizing the KI aggregate) did not have sufficient sample density to determine morphology via EM. Although this short-lived kinetic intermediate shares similarities to the **1a** DWNTs in lineshape and slightly blueshifted absorbance, we do not label it definitively as DWNT out of caution.

Thus, increasing the length of the polymethine bridge has a strong effect on the supramolecular packing of these chromophores. Trimethines **1a** and **1b** clearly have a propensity to form individual DWNTs, which slowly interconvert into bundles over many weeks, while

pentamethines **2a** and **2b** rapidly form bundles within minutes.²⁶ We hypothesize that the pentamethine dyes aggregate into bundles more readily due to the increase in size, hydrophobicity, and polarizability. Additionally, bundles are the overall thermodynamic minimum of these aggregates, and therefore stronger non-covalent interactions in the assembly may imply a lower barrier to bundle formation. Overall, we observed only minor differences in the aggregates formed from **2a** and **2b**, most notably broader linewidths for the brominated dyes, suggesting a higher level of disorder in the **2b** nanostructures.

Following the identification of the various aggregate morphologies, we probed the photophysical properties of **2a** and **2b** in comparison to **1a** and **1b** (Table 1). We used quantum yields (QY, Φ_F), energy gaps (E_g), and fluorescence lifetimes (τ) to obtain the transition dipole moment (TDM, μ) for each compound's electronic transitions, as well as each aggregate morphology's excitonic transitions. The emission spectra of **2a** are shown in Figure 3a, as well as the lifetimes and fittings in Figure 3b. A full explanation of the photophysical characterization and derivation of TDM can be found in SI Sections 7-9, and in Table 1.

The transition dipole moments for all monomers and aggregates are detailed in Figure 3c. Using these TDM values, we calculated the superradiance parameter η_{SR} for each dye, as shown in equation 1.

$$\eta_{SR} = \frac{\mu_{agg}^2}{\mu_{mon}^2} = \frac{k_{r,agg} E_{g,mon}^3}{k_{r,mon} E_{g,agg}^3} \quad (\text{Eq 1})$$

Although other works have used different definitions for superradiance in J-aggregate systems^{14,36,37}, we maintain that this method factors in the difference in energy gap, which by itself gives rise to an intrinsic change in radiative rates due to the redshift from monomer to aggregate.³⁸

The η_{SR} parameter is also a measure of the coherence length for the fluorescent state, or the number of monomers over which the Frenkel excitons delocalize.³⁹

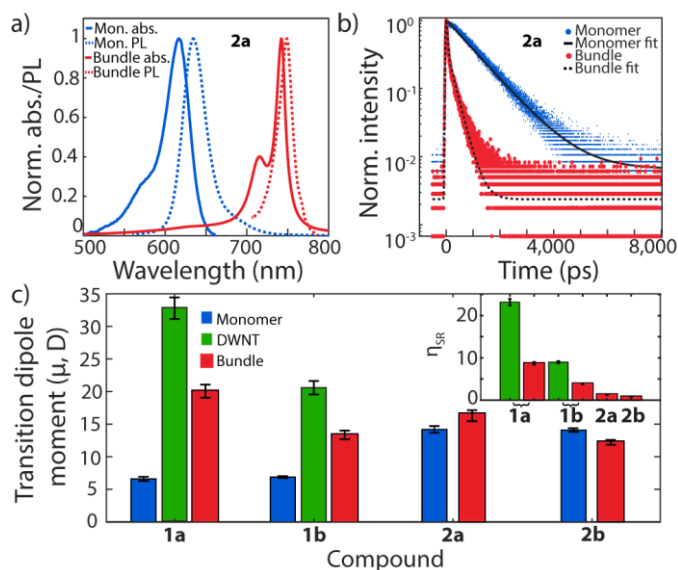


Figure 3. Photophysical characterization of monomers and aggregates of 2a/2b. a) Absorption (solid) and photoluminescence (dotted) spectra for **2a** monomer (methanol) and bundle (methanol/water). b) Monomer lifetime, bundle lifetime, and corresponding fits for **2a**. c) Transition dipole moments for all monomers (blue) and aggregate morphologies (green, red). (Inset: superradiance parameter η_{SR} for each aggregate morphology.)

Figure 3c demonstrates that the trimethine aggregates possess transition dipole moments up to 5 times larger than their monomer counterparts; this corresponds to high superradiance parameters (e.g. ~ 23 for **1a** DWNT). However, for the pentamethine dyes, the aggregate transition dipoles are comparable to those of the monomers. This accordingly leads to η_{SR} values that are closer to 1, meaning that they are less superradiant (or in the case of **2b**, subradiant). These data can be attributed to the higher disorder in aggregates of **2a** and **2b** which leads to decreased exciton delocalization despite retaining redshifted emission. We also observe that the brominated aggregates are less superradiant than their chlorinated counterparts; we hypothesize this is due to the additional energetic disorder, which is indicated by the broader absorption linewidths and also via qualitative estimates of structural disorder in the cryo-EM.

Table 1. Photophysical data for monomers and aggregates of dyes **1a**, **1b**, **2a**, and **2b**. Quantum yield (Φ_F) error was taken as the standard deviation of triplicate measurements. Lifetime (τ) error was taken from the 95% confidence interval in fitting. Error in radiative rate (k_r) and superradiance parameter (η_{SR}) were propagated from the original lifetime and quantum yield measurements.

Dye	Morphology	Φ_F	Avg. τ (ps)	$k_r * 10^8$ (s ⁻¹)	E_g (nm)	μ (D)	η_{SR}
1a	Monomer	0.025 ± 0.002	202 ± 1	1.2 ± 0.1	528	6.8 ± 0.3	
1a	DWNT	0.15 ± 0.020^a	140 ± 2	20 ± 2	597	33 ± 2	23.2 ± 0.8
1a	Bundle	0.036 ± 0.004	81 ± 1	7.3 ± 0.7	602	20 ± 1	8.7 ± 0.3
1b	Monomer	0.028 ± 0.002	220 ± 1	1.3 ± 0.1	530	6.9 ± 0.1	
1b	DWNT	0.040 ± 0.004^a	68 ± 2	8.1 ± 0.7	593	21 ± 1	9.0 ± 0.2
1b	Bundle	0.013 ± 0.001	62 ± 1	3.2 ± 0.3	603	13.4 ± 0.7	3.8 ± 0.1
2a	Monomer	0.33 ± 0.025	1019 ± 3	3.3 ± 0.2	625	14.2 ± 0.5	
2a	Bundle	0.012 ± 0.001	72 ± 2	2.6 ± 0.3	740	16.3 ± 0.9	1.3 ± 0.1
2b	Monomer	0.36 ± 0.020	1126 ± 2	3.2 ± 0.2	623	14.1 ± 0.4	
2b	Bundle	0.006 ± 0.001	70 ± 1	1.6 ± 0.2	725	12.2 ± 0.6	0.8 ± 0.1

^aValues taken from literature.^{31,40}

We employed computational screening to gauge how tube radii, chiral angle, and slip between monomer units affect resultant spectral properties, and in order to estimate a structure consistent with the excitonic result.^{8,41-43} For simplicity, we focus on bundles derived from dyes **1a** and **2a**, though these results likely generalize. In Table 2, we report the experimentally determined tube radii and relative and absolute energies/heights of the parallel and perpendicular transition. In comparing values between aggregates, while similar overall shifts, we observe differences in peak ratios and parallel to perpendicular shifts.

Table 2. Experimental observables used for tube-wrapping computations. Tube radii were taken from cryo-EM, absorption shifts were taken from spectra of **1a** and **2a** monomers and aggregates at 75K. Chiral angles were computed using the ratio of peaks and shift in the zero-disorder limit, see SI section 10.

Dye Bundles	\parallel to \perp Height Ratio	Monomer to \parallel shift (cm^{-1})	\parallel to \perp shift (cm^{-1})	Average tube radius (\AA)	Chiral Angle ($^\circ$)
1a	0.71	-2573	658	44	± 40
2a	0.44	-2793	506	23	± 33

To construct model aggregates and determine their spectral properties we begin by asserting that the bundles are comprised of weakly coupled single-walled nanotubes.²⁶ Lattice brick dimensions were determined by adding 2 \AA of slip to the Cl-Cl distance across the dye following prior work.⁴⁴ Potential tube structures (and thus Hamiltonians) were determined using a planar lattice with a variable slip between bricks. Furthermore, we only considered only chiral angles that permit tubular radii within 1 \AA of the measured value. Figure 4a shows examples of valid tube rolling parameters starting from a 2D planar lattice of aggregates of **2a**. Packing geometries that generate tubes of radii within the set tolerance are demarcated by red crosses.

The polar plots in Figure 4b visualize the extended screening approach with the distance from the origin indicating slip and polar angle (θ) indicating chiral wrapping. To handle many realizations of slip, chiral angle and diagonal disorder, we employed a stochastic method for estimating optical observables described in prior publications.⁴³ Within 4b, the left half of the polar plot shows the position of the tube parallel absorption peak relative shift relative to the monomer. The color of each state corresponds to the degree of spectral shift, i.e. redshifted parallel absorption in J- (and I-) aggregates, and blueshifted parallel absorption in H-aggregates. On the right half of the polar plot, we use yellow to mark all simulations that give a valid match to the experimental 75 K absorption spectra for the ratio of absorption shifts between parallel and perpendicular peaks, $(E_{\perp} - E_{mon}) / (E_{\parallel} - E_{mon})$. We further reduce the space by estimating the chiral angle based on the ratio of parallel and perpendicular peak heights (see SI section 10), which yielded a value of ± 40 and ± 33 degrees (reported in Table 2). We then performed a close screening ± 10 degrees

from the predicted value denoted by the shaded blue region on the right side of Figures 4b and 4c. Similar to our previous work, we scanned all possible slips excluding the range of 0-2 Å, where H-aggregation predominates.⁴⁴

Using the best fit solutions generated in Figure 4b/c, we generated spectra by implementing different amounts of diagonal disorder until we showed agreement with the FWHM of the experimental absorption spectra. The slip value and chiral angle between bundles of **1a** and **2a** dyes are consistent (24° vs. 30.4° and 6.15 Å vs. 5.5 Å, respectively). Interestingly, the differences in spectra seem to only arise due to differences in tube width. The apparent small differences in slip and chiral angle may only arise due to the increased length of the monomer unit, which subsequently influences packing.

Our results demonstrate how decreased tube widths and stronger dipolar coupling can mask higher disorder. As Figure 4c shows, bundles of **2a** have a larger space of allowed slips and chiral angles that produce ~3,000 cm⁻¹ of redshift relative to both in slip and the chiral angle also appears to have less influence on the redshift of the parallel peak in the simulations of **2a**. Our model shows that narrower tube widths result in a more quasi-one-dimensional system leading to chiral angle only weakly influencing resultant spectral features. Additionally, modelling the absorption spectra of the **2a** bundles required that we include nearly twice the disorder (560 cm⁻¹), as opposed to 220 cm⁻¹ for the bundles of **1a**. Despite similar ending linewidths for **1a** and **2a** bundles, this increased disorder likely matches the qualitative observation of increased structural disorder under cryo-EM and decreased superradiance observed for the **2a/2b** bundles.

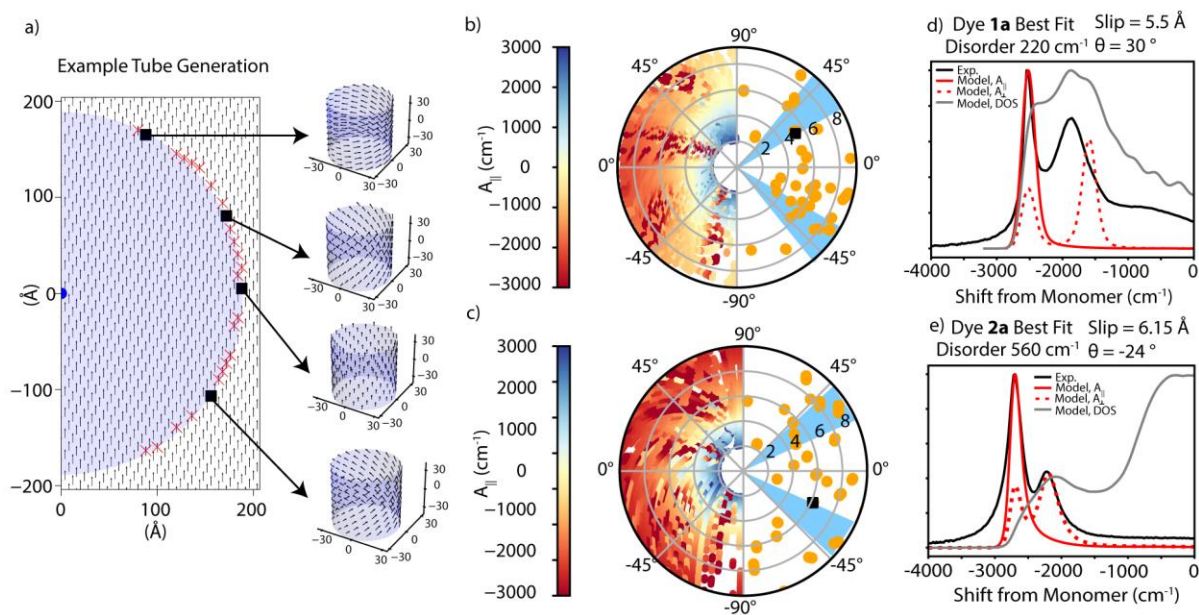


Figure 4. **a)** Examples of the tube-wrapping simulation used for bundles of **2a**. **b,c)** Polar plots of **1a** (**b**) and **2a** (**c**) visualizing the computational screening conditions of slip and chiral angle used to find matches between the monomer to aggregate shift and relative ratios of aggregate peaks. The degree of blue/redshift for each slip/chiral angle is given on the left side of the plot. The space of possible solutions screened (right side) is shaded in blue, with yellow dots indicating possible solutions, and a black dot indicating the best match to experimental data. **d,e)** Experimental and modelled absorption spectra/DOS of **1a** (**d**) and **2a** (**e**) from screening fits shown in Figure 4b.

We note that the energy difference between parallel and perpendicular peaks changes between the bundles of **1a** and **2a**. While our model accurately describes absorption spectra of the **2a** bundles, it somewhat fails to capture the peak separations for **1a**; we hypothesize this is the result of inter-tube coupling. Previous work has predicted that inter-tube coupling can only effect the perpendicular peak due to the coupling of parallel long-wavelength excitations only producing boundary charges on the aggregate.⁴⁵ Ultimately, we learn that the largest differences in excitonic aggregate properties seem to arise from the individual tube width; the **2a** and **2b** tubes are roughly twice as thin as the **1a** and **1b** tubes, implying that the bundles of **2a** and **2b** contain fewer dyes wrapping around the cylinder.

Overall, the modelling indicates that the changes in tube width lead to changes in the relative energies of the excitonic states, as well as the amount of disorder required to realize the experimental spectrum. Building upon our qualitative estimates of disorder from cryo-EM, it seems the thinner tubes yield less consistent packing and assemble into more disordered structures, potentially due to the more varied solutions of slip and chiral angle shown in Figure 4b. These differences also demonstrate how radical changes in self-assembly can stem from only small modifications to the monomer building block.

Conclusion

We synthesized and aggregated two new pentamethine dyes based on the C8S3 scaffold to create two new emitters at ~ 750 nm. We maintain the lineshapes of the original aggregates while redshifting by 100 nm and found with cryo-EM imaging that the pentamethine dyes mainly self-assembled into large bundles of nanotubes, as opposed to long single or double-walled tubes. Photophysical characterization of these aggregates then allowed us to calculate transition dipole moments and superradiance parameters for each compound and aggregate morphology. Correlating the morphological and photophysical data, we were able to conclude that the pentamethine dyes displayed different kinetics of self-assembly that resulted in generally more disordered aggregate bundles with lower superradiance relative to their trimethine comparators. We employed computational screening to examine how structural differences between the trimethine and pentamethine aggregates affect their excitonic properties, finding that the primary differences in spectral characteristics arise from differences in tube widths as compared to the trimethine counterparts.

There are several key takeaways from our study. Initial screens showed highly redshifted aggregate structures in the pentamethine dye series that analogized easily to the prior observed

trimethine bundles. However, despite similar spectral features (including a nearly matching overall redshifts and peak positions) more detailed photophysical analysis revealed that a significant decline in superradiance. Computational screening showed that we could reproduce the shifts and peak positions while invoking higher diagonal disorder, and that the primary difference between the dyes arises from the smaller tubular radii. Indeed, the smaller tubular radii results in a quasi-1D density of excitonic states that serves to create increased dipolar coupling, while masking structural/diagonal disorder which leads to decreased superradiance. In short, while amphiphilic dyes can be coaxed to form tubular aggregates, the properties that give rise to superradiant excitons are more sensitive to the conditions of assembly.

Acknowledgements

This work was supported by NSF CHE-1905242, NSF CHE-2204263, NSF CHE-1763176, and NSF CHE-1048804. NCB was supported by NSF Graduate Research Fellowship Program, DGE-2034835. The authors acknowledge the use of instruments at the Electron Imaging Center for NanoMachines supported by the NIH (1S10RR23057) and CNSI at UCLA.

References

- (1) Bricks, J. L.; Slominskii, Y. L.; Panas, I. D.; Demchenko, A. P. Fluorescent J-Aggregates of Cyanine Dyes: Basic Research and Applications Review. *Methods Appl. Fluoresc.* **2017**, *6* (1), 012001. <https://doi.org/10.1088/2050-6120/AA8D0D>.
- (2) Würthner, F.; Kaiser, T. E.; Saha-Möller, C. R. J-Aggregates: From Serendipitous Discovery to Supramolecular Engineering of Functional Dye Materials. *Angew. Chem. Int. Ed.* **2011**, *50* (15), 3376–3410. <https://doi.org/10.1002/ANIE.201002307>.
- (3) Sun, C.; Li, B.; Zhao, M.; Wang, S.; Lei, Z.; Lu, L.; Zhang, H.; Feng, L.; Dou, C.; Yin, D.; Xu, H.; Cheng, Y.; Zhang, F. J-Aggregates of Cyanine Dye for NIR-II in Vivo Dynamic Vascular Imaging beyond 1500 Nm. *J. Am. Chem. Soc.* **2019**, *141* (49), 19221–19225. <https://doi.org/10.1021/JACS.9B10043>.
- (4) Shakiba, M.; Ng, K. K.; Huynh, E.; Chan, H.; Charron, D. M.; Chen, J.; Muhanna, N.; Foster, F. S.; Wilson, B. C.; Zheng, G. Stable J-Aggregation Enabled Dual Photoacoustic and Fluorescence Nanoparticles for Intraoperative Cancer Imaging. *Nanoscale* **2016**, *8* (25), 12618–12625. <https://doi.org/10.1039/C5NR08165C>.

- (5) Saito*, K. Quenching of Excited J Aggregates on Metals by Surface Plasmon Excitations. *J. Phys. Chem. B* **1999**, *103* (31), 6579–6583. <https://doi.org/10.1021/JP991082K>.
- (6) Brixner, T.; Hildner, R.; Köhler, J.; Lambert, C.; Würthner, F. Exciton Transport in Molecular Aggregates – From Natural Antennas to Synthetic Chromophore Systems. *Adv. Energy Mater.* **2017**, *7* (16), 1700236. <https://doi.org/10.1002/AENM.201700236>.
- (7) Hans von Berlepsch, *, †; Stefan Kirstein, ‡ and; Böttcher†, C. Supramolecular Structure of J-Aggregates of a Sulfonate Substituted Amphiphilic Carbocyanine Dye in Solution: Methanol-Induced Ribbon-to-Tubule Transformation. *J. Phys. Chem. B* **2004**, *108* (48), 18725–18733. <https://doi.org/10.1021/JP046546F>.
- (8) Deshmukh, A. P.; Koppel, D.; Chuang, C.; Cadena, D. M.; Cao, J.; Caram, J. R. Design Principles for Two-Dimensional Molecular Aggregates Using Kasha’s Model: Tunable Photophysics in Near and Short-Wave Infrared. **2019**. <https://doi.org/10.1021/acs.jpcc.9b05060>.
- (9) Engel, G. S.; Calhoun, T. R.; Read, E. L.; Ahn, T. K.; Mančal, T.; Cheng, Y. C.; Blankenship, R. E.; Fleming, G. R. Evidence for Wavelike Energy Transfer through Quantum Coherence in Photosynthetic Systems. *Nature* **2007**, *446* (7137), 782–786. <https://doi.org/10.1038/nature05678>.
- (10) Scholes, G. D.; Fleming, G. R.; Olaya-Castro, A.; Van Grondelle, R. Lessons from Nature about Solar Light Harvesting. *Nature Chemistry*. Nature Publishing Group October 23, 2011, pp 763–774. <https://doi.org/10.1038/nchem.1145>.
- (11) Freyria, F. S.; Cordero, J. M.; Caram, J. R.; Doria, S.; Dodin, A.; Chen, Y.; Willard, A. P.; Bawendi, M. G. Near-Infrared Quantum Dot Emission Enhanced by Stabilized Self-Assembled J-Aggregate Antennas. *Nano Lett.* **2017**, *17* (12), 7665–7674. <https://doi.org/10.1021/ACS.NANOLETT.7B03735>.
- (12) Caram, J. R.; Engel, G. S. Extracting Dynamics of Excitonic Coherences in Congested Spectra of Photosynthetic Light Harvesting Antenna Complexes. *Faraday Discuss.* **2011**, *153* (0), 93–104. <https://doi.org/10.1039/C1FD00049G>.
- (13) Wang, C.; Weiss, E. A. Accelerating FRET between Near-Infrared Emitting Quantum Dots Using a Molecular J-Aggregate as an Exciton Bridge. *Nano Lett.* **2017**, *17* (9), 5666–5671. <https://doi.org/10.1021/ACS.NANOLETT.7B02559>.
- (14) Doria, S.; Sinclair, T. S.; Klein, N. D.; Bennett, D. I. G.; Chuang, C.; Freyria, F. S.; Steiner, C. P.; Foggi, P.; Nelson, K. A.; Cao, J.; Aspuru-Guzik, A.; Lloyd, S.; Caram, J. R.; Bawendi, M. G. Photochemical Control of Exciton Superradiance in Light-Harvesting Nanotubes. *ACS Nano* **2018**, *12* (5), 4556–4564. <https://doi.org/10.1021/acs.nano.8b00911>.
- (15) Chuang, C.; Lee, C. K.; Moix, J. M.; Knoester, J.; Cao, J. Quantum Diffusion on Molecular Tubes: Universal Scaling of the 1D to 2D Transition. **2016**. <https://doi.org/10.1103/PhysRevLett.116.196803>.
- (16) Berlepsch, H. v.; Böttcher, C. Tubular J-Aggregates of a New Thiocarbocyanine Cy5 Dye for the Far-Red Spectral Region – a Spectroscopic and Cryo-Transmission Electron Microscopy Study. *Phys. Chem. Chem. Phys.* **2018**, *20* (28), 18969–18977. <https://doi.org/10.1039/C8CP03378A>.
- (17) Chen, Z.; Liu, Y.; Wagner, W.; Stepanenko, V.; Ren, X.; Ogi, S.; Würthner, F. Near-IR Absorbing J-Aggregate of an Amphiphilic BF2-Azadipyromethene Dye by Kinetic Cooperative Self-Assembly. *Angew. Chem. Int. Ed.* **2017**, *56* (21), 5729–5733. <https://doi.org/10.1002/ANIE.201701788>.

- (18) Wenus, J.; Ceccarelli, S.; Lidzey, D. G.; Tolmachev, A. I.; Slominskii, J. L.; Bricks, J. L. Optical Strong Coupling in Microcavities Containing J-Aggregates Absorbing in near-Infrared Spectral Range. *Org. Electron.* **2007**, *8* (2–3), 120–126. <https://doi.org/10.1016/J.ORGEL.2006.06.006>.
- (19) Hilderbrand, S. A.; Weissleder, R. Near-Infrared Fluorescence: Application to in Vivo Molecular Imaging. *Curr. Opin. Chem. Biol.* **2010**, *14* (1), 71–79. <https://doi.org/10.1016/J.CBPA.2009.09.029>.
- (20) Lim, Y. T.; Kim, S.; Nakayama, A.; Stott, N. E.; Bawendi, M. G.; Frangioni, J. V. Selection of Quantum Dot Wavelengths for Biomedical Assays and Imaging: *Mol. Imaging* **2003**, *2* (1), 50–64. <https://doi.org/10.1162/15353500200302163>.
- (21) Rondão, R.; Frias, A. R.; Correia, S. F. H.; Fu, L.; Bermudez, V. de Z.; André, P. S.; Ferreira, R. A. S.; Carlos, L. D. High-Performance Near-Infrared Luminescent Solar Concentrators. *ACS Appl. Mater. Interfaces* **2017**, *9* (14), 12540–12546. <https://doi.org/10.1021/ACSAMI.7B02700>.
- (22) Pawlik, A.; Kirstein, S.; De Rossi, U.; Daehne, S. Structural Conditions for Spontaneous Generation of Optical Activity in J-Aggregates. *J Phys Chem B* **1997**, *101*, 5646–5651.
- (23) Eisele, D. M.; Cone, C. W.; Bloemsmas, E. A.; Vlaming, S. M.; Van Der Kwaak, C. G. F.; Silbey, R. J.; Bawendi, M. G.; Knoester, J.; Rabe, J. P.; Vanden Bout, D. A. Utilizing Redox-Chemistry to Elucidate the Nature of Exciton Transitions in Supramolecular Dye Nanotubes. *Nat. Chem.* **2012**, *4* (8), 655–662. <https://doi.org/10.1038/nchem.1380>.
- (24) Eisele, D. M.; Knoester, J.; Kirstein, S.; Rabe, J. P.; Vanden Bout, D. A. Uniform Exciton Fluorescence from Individual Molecular Nanotubes Immobilized on Solid Substrates. *Nat. Nanotechnol.* **2009**, *4* (10), 658–663. <https://doi.org/10.1038/nnano.2009.227>.
- (25) Jennifer L. Lyon, †; Dörthe M. Eisele, ‡; Stefan Kirstein, ‡; Jürgen P. Rabe, ‡; David A. Vanden Bout, † and; Keith J. Stevenson*, †. Spectroelectrochemical Investigation of Double-Walled Tubular J-Aggregates of Amphiphilic Cyanine Dyes. *J. Phys. Chem. C* **2008**, *112* (4), 1260–1268. <https://doi.org/10.1021/JP077412F>.
- (26) Eisele, D. M.; Arias, D. H.; Fu, X.; Bloemsmas, E. A.; Steiner, C. P.; Jensen, R. A.; Rebentrost, P.; Eisele, H.; Tokmakoff, A.; Lloyd, S.; Nelson, K. A.; Nicastro, D.; Knoester, J.; Bawendi, M. G. Robust Excitons Inhabit Soft Supramolecular Nanotubes. *Proc. Natl. Acad. Sci. U. S. A.* **2014**, *111* (33), E3367–E3375. <https://doi.org/10.1073/pnas.1408342111>.
- (27) Ng, K.; Webster, M.; Carbery, W. P.; Visaveliya, N.; Gaikwad, P.; Jang, S. J.; Kretschmar, I.; Eisele, D. M. Frenkel Excitons in Heat-Stressed Supramolecular Nanocomposites Enabled by Tunable Cage-like Scaffolding. *Nat. Chem.* **2020**, *12* (12), 1157–1164. <https://doi.org/10.1038/s41557-020-00563-4>.
- (28) Caram, J. R.; Doria, S.; Eisele, D. M.; Freyria, F. S.; Sinclair, T. S.; Rebentrost, P.; Lloyd, S.; Bawendi, M. G. Room-Temperature Micron-Scale Exciton Migration in a Stabilized Emissive Molecular Aggregate. *Nano Lett.* **2016**, *16* (11), 6808–6815. <https://doi.org/10.1021/acs.nanolett.6b02529>.
- (29) Yuen-Zhou, J.; Arias, D. H.; Eisele, D. M.; Steiner, C. P.; Krich, J. J.; Bawendi, M. G.; Nelson, K. A.; Aspuru-Guzik, A. Coherent Exciton Dynamics in Supramolecular Light-Harvesting Nanotubes Revealed by Ultrafast Quantum Process Tomography. *ACS Nano* **2014**, *8* (6), 5527–5534. <https://doi.org/10.1021/NN406107Q>.

- (30) Kriete, B.; Lüttig, J.; Kunsel, T.; Malý, P.; Jansen, T. L. C.; Knoester, J.; Brixner, T.; Pshenichnikov, M. S. Interplay between Structural Hierarchy and Exciton Diffusion in Artificial Light Harvesting. <https://doi.org/10.1038/s41467-019-12345-9>.
- (31) Rn Kriete, B.; Bondarenko, A. S.; Jumde, V. R.; Franken, L. E.; Minnaard, A. J.; Jansen, T. L. C.; Knoester, J.; Pshenichnikov, M. S. Steering Self-Assembly of Amphiphilic Molecular Nanostructures via Halogen Exchange. *J Phys Chem Lett* **2017**. <https://doi.org/10.1021/acs.jpcllett.7b00967>.
- (32) Roth, S. M.; Press, D. J.; Heyne, B.; Sutherland, T. C. Synthetic Access to Benzimidacarbocyanine Dyes to Tailor Their Aggregation Properties. *J. Org. Chem.* **2021**, *86*, 8651. <https://doi.org/10.1021/ACS.JOC.1C00385>.
- (33) Bricks, J. L.; Kachkovskii, A. D.; Slominskii, Y. L.; Gerasov, A. O.; Popov, S. V. Molecular Design of near Infrared Polymethine Dyes: A Review. *Dyes and Pigments*. 2015. <https://doi.org/10.1016/j.dyepig.2015.05.016>.
- (34) Clark, K. A.; Cone, C. W.; Bout, D. A. Vanden. Quantifying the Polarization of Exciton Transitions in Double-Walled Nanotubular J-Aggregates. *J Phys Chem C* **2013**, *117* (50), 26473–26481. <https://doi.org/10.1021/jp409573h>.
- (35) Deshmukh, A. P.; Bailey, A. D.; Forte, L. S.; Shen, X.; Geue, N.; Sletten, E. M.; Caram, J. R. Thermodynamic Control over Molecular Aggregate Assembly Enables Tunable Excitonic Properties across the Visible and Near-Infrared. *J. Phys. Chem. Lett.* **2020**, *11* (19), 8026–8033. <https://doi.org/10.1021/acs.jpcllett.0c02204>.
- (36) Akins, D. L. Superradiance of Aggregated Thiocarbocyanine Molecules. **1999**. <https://doi.org/10.1021/jp991627a>.
- (37) Zhao, H.; Zhao, Y.; Song, Y.; Zhou, M.; Lv, W.; Tao, L.; Feng, Y.; Song, B.; Ma, Y.; Zhang, J.; Xiao, J.; Wang, Y.; Lien, D.-H.; Amani, M.; Kim, H.; Chen, X.; Wu, Z.; Ni, Z.; Wang, P.; Shi, Y.; Ma, H.; Zhang, X.; Xu, J.-B.; Troisi, A.; Javey, A.; Wang, X. Strong Optical Response and Light Emission from a Monolayer Molecular Crystal. *Nat. Commun.* **2019**, *10* (1), 1–9. <https://doi.org/10.1038/s41467-019-13581-9>.
- (38) Friedman, H.; Cosco, E.; Atallah, T.; Jia, S.; Sletten, E.; Caram, J. Establishing Design Principles for Emissive Organic SWIR Chromophores from Energy Gap Laws. *Chem* **2021**, *7*, 1–18. <https://doi.org/10.26434/CHEMRXIV.14374493.V1>.
- (39) Tsurumi, T.; Hirayama, H.; Vacha, M.; Taniyama, T. *Nanoscale Physics for Materials Science*; Taylor & Francis: Abingdon, 2010.
- (40) Freyria, F. S.; Cordero, J. M.; Caram, J. R.; Doria, S.; Dodin, A.; Chen, Y.; Willard, A. P.; Bawendi, M. G. Near-Infrared Quantum Dot Emission Enhanced by Stabilized Self-Assembled J-Aggregate Antennas. *Nano Lett.* **2017**, *17* (12), 7665–7674. <https://doi.org/10.1021/ACS.NANOLETT.7B03735>.
- (41) Didraga, C.; Klugkist, J. A.; Knoester, J. Optical Properties of Helical Cylindrical Molecular Aggregates: The Homogeneous Limit. *J. Phys. Chem. B* **2002**, *106* (44), 11474–11486. <https://doi.org/10.1021/JP026217S/ASSET/IMAGES/LARGE/JP026217SF00007.JPEG>.
- (42) Didraga, C.; Pugžlys, A.; Hania, P. R.; Von Berlepsch, H.; Duppen, K.; Knoester, J. Structure, Spectroscopy, and Microscopic Model of Tubular Carbocyanine Dye Aggregates. *J. Phys. Chem. B* **2004**, *108* (39), 14976–14985. <https://doi.org/10.1021/JP048288S/ASSET/IMAGES/MEDIUM/JP048288SE00023.GIF>.

- (43) *Stochastically Realized Observables for Excitonic Molecular Aggregates* / *The Journal of Physical Chemistry A*. <https://pubs.acs.org/doi/10.1021/acs.jpca.0c07953> (accessed 2022-09-05).
- (44) Deshmukh, A. P.; Geue, N.; Bradbury, N. C.; Atallah, T. L.; Chuang, C.; Pengshung, M.; Cao, J.; Sletten, E. M.; Neuhauser, D.; Caram, J. R. Bridging the Gap between H- and J-Aggregates: Classification and Supramolecular Tunability for Excitonic Band Structures in Two-Dimensional Molecular Aggregates. *Chem. Phys. Rev.* **2022**, 3 (2), 021401. <https://doi.org/10.1063/5.0094451>.
- (45) Chuang, C.; Knoester, J.; Cao, J. Scaling Relations and Optimization of Excitonic Energy Transfer Rates between One-Dimensional Molecular Aggregates. *J. Phys. Chem. B* **2014**, 118 (28), 7827–7834. <https://doi.org/10.1021/jp4124502>.